Research Square

Preprints are preliminary reports that have not undergone peer review.
They should not be considered conclusive, used to inform clinical practice,
or referenced by the media as validated information.

Dispersion-Engineered SOI Ridge Waveguides for Broadband Nonlinear Photonics and Polarization-Insensitive Transport

Reza Goodarzi

rego.physics@gmail.com

Laser, Photonics and Quantum Research School, Nuclear Science and Technology Research Institute (NSTRI), Atomic Energy Organization of Iran

Research Article

Keywords: Silicon-on-insulator, Ridge Waveguide, Semi-analytical Modeling, Numerical Simulation, Dispersion Engineering, Supercontinuum Generation, Kerr Frequency Combs, Two-Photon Absorption, Polarization Insensitivity, Thermal Dissipation

Posted Date: October 8th, 2026

DOI: https://doi.org/10.21203/rs.3.rs-11101998/v1

License: This work is licensed under a Creative Commons Attribution 4.0 International License.
Read Full License

Additional Declarations: No competing interests reported.

Dispersion-Engineered SOI Ridge Waveguides for Broadband Nonlinear Photonics and Polarization-Insensitive Transport

Reza Goodarzi

Laser, Photonics and Quantum Research School, Nuclear Science and Technology Research Institute (NSTRI), Atomic Energy Organization of Iran, Tehran, Iran

E-mail: rego.physics@gmail.com

Abstract Sub-micron silicon-on-insulator (SOI) strip waveguides face a well-known dilemma: strong optical confinement comes at the price of steep normal dispersion, high sidewall scattering, and severe modal birefringence. Here, we show how partial etching into a ridge geometry resolves these constraints across two distinct operating regimes. We combine calibrated full-vector modal solvers, layout synthesis, beam-propagation electrodynamics, and nonlinear pulse propagation into a unified computational model. For nonlinear applications, Platform A ($W = 480$ nm, $H = 220$ nm, $h_{\mathrm{slab}} = 65$ nm) flattens the group-velocity dispersion, delivering anomalous values ($D = +18.0$ ps/(nm·km), $\beta_2 = -23$ ps^2/km at 1550 nm) across 1420–1680 nm inside a broad $|D| \leq 18$ ps/(nm·km) window (1400–1700 nm). This profile supports a 267-nm four-wave mixing gain bandwidth at $P_p = 650$ mW, near-octave supercontinuum generation (1150–2200 nm) under 100-fs pulse pumping, and single-soliton Kerr combs (79 lines across 17.7 THz, FSR = 227.2 GHz) at $P_{\mathrm{in}} = 12.5$ mW when accounting for carrier kinetics and cavity heating via the Lugiato–Lefever equation. Conversely, Platform B ($W = 570$ nm, $H = 400$ nm, $h_{\mathrm{slab}} = 127$ nm) addresses polarization sensitivity. It suppresses phase birefringence below $|\Delta n_{\mathrm{eff}}| < 10^{-6}$ and limits group birefringence to $|\Delta n_g| < 1.5 \times 10^{-5}$, holding differential group delay under 0.50 fs/cm with single-mode guidance throughout the C-band. Tapered mode converters maintain insertion losses below 0.15 dB with reflections under −42 dB. Three-dimensional volume current calculations indicate a 58% drop in sidewall scattering relative to wire baselines ($\alpha_{\mathrm{scat}} = 1.14 \pm 0.08$ dB/cm vs. 2.70 ± 0.15 dB/cm). Both cross-sections tolerate standard lithographic errors ($\Delta W = \pm 10$ nm, $\Delta h_{\mathrm{slab}} = \pm 5$ nm) and align with air-clad silicon manufacturing.

Keywords Silicon-on-insulator · Ridge Waveguide · Semi-analytical Modeling · Numerical Simulation · Dispersion Engineering · Supercontinuum Generation · Kerr Frequency Combs · Two-Photon Absorption · Polarization Insensitivity · Thermal Dissipation.

1 Introduction

Silicon-on-insulator (SOI) waveguides pack intense optical fields into sub-micron cross sections. The large refractive index step between the silicon core ($n_{\mathrm{Si}} \approx 3.476$ at 1550 nm) and the silica substrate ($n_{\mathrm{SiO_2}} \approx 1.444$) provides sub-wavelength modal confinement [1–5]. Paired with silicon's electronic Kerr coefficient ($n_2 \approx 4.5 \times 10^{-18}$ m^2/W), this tight confinement elevates the effective waveguide nonlinearity above $\gamma > 100$ W^{-1}m^{-1} ($\gamma > 10^5$ W^{-1}km^{-1}). Such values open direct routes to chip-scale four-wave mixing (FWM), self-phase modulation (SPM), dissipative Kerr solitons (DKS), and broadband supercontinuum generation (SCG) at moderate drive powers [6–12].

Conventional fully etched strip wires, however, hit sharp physical roadblocks. Their group-velocity dispersion (GVD) is strongly normal, routinely falling below $D < -800$ ps/(nm·km) near telecommunication wavelengths. This steep normal dispersion ruins phase matching for parametric processes and rules out bright soliton formation. Wire waveguides also suffer from heavy sidewall scattering losses ($\alpha > 2.5$ dB/cm) because the optical mode overlaps directly with vertical roughness left by reactive-ion etching [13,14]. Structural asymmetry introduces substantial modal birefringence ($\Delta n_{\mathrm{eff}} = n_{\mathrm{eff,TE}} - n_{\mathrm{eff,TM}} \neq 0$), triggering polarization-dependent delays that distort polarization-division multiplexed signals.

Shifting from a strip to a ridge (rib) architecture alters these boundary conditions. Leaving a thin unetched silicon slab of thickness h_{slab} allows guided light to expand laterally. This geometric modification counteracts silicon's intrinsic material dispersion, flattening the GVD into a low-dispersion window ($|D| \leq 18$ ps/(nm·km)) with an anomalous band between 1420 and 1680 nm [15–17,33]. Pulling the peak intensity toward the waveguide center reduces field contact with etched sidewalls, cutting scattering losses by over half compared to standard strip baselines [18]. Balancing the horizontal and vertical modal dimensions can elimi-

nate phase birefringence ($\Delta n_{\text{eff}} \approx 0$) while driving group birefringence toward zero ($\Delta n_g \approx 0$) at 1550 nm [19,20].

Turning these theoretical concepts into functional devices requires coordinated modeling across multiple physical domains. Here, we build a coupled computational workflow that connects modal dispersion, layout synthesis, electrodynamic propagation, and nonlinear time-domain kinetics. The model pairs a three-oscillator Sellmeier engine with full-vector finite-element modal solutions. It incorporates lithographic layouts for strip-to-ridge mode converters and microrings, verifies taper transmission ($S_{21} > -0.15$ dB) and reflection ($S_{11} < -42$ dB) through beam-propagation electrodynamics, and simulates pulse evolution using the Generalized Nonlinear Schrödinger Equation (GNLSE) with higher-order dispersion (β_2–β_8), two-photon absorption (TPA), free-carrier effects (FCA/FCD), and Raman scattering ($f_R = 0.043$). We model Kerr microcomb formation via the spatiotemporal Lugiato–Lefever Equation (LLE) with carrier and thermal feedback, and quantify sidewall scattering using the three-dimensional Vector Volume Current Method (VCM).

We examine two tailored platforms. Platform A ($W = 480$ nm, $H = 220$ nm, $h_{\text{slab}} = 65$ nm) targets nonlinear devices. It provides anomalous GVD ($D > 0$, $\beta_2 = -23$ ps^2/km) across 1420–1680 nm inside a low-dispersion span ($|D| \leq 18$ ps/(nm·km), 1400–1700 nm), yielding a 267-nm FWM gain bandwidth, near-octave SCG (1150–2200 nm), and 79-line Kerr combs. Platform B ($W = 570$ nm, $H = 400$ nm, $h_{\text{slab}} = 127$ nm) serves polarization-insensitive routing. It achieves phase-birefringence cancellation ($|\Delta n_{\text{eff}}| < 10^{-6}$) at 1550 nm with $|\Delta n_g| < 1.5 \times 10^{-5}$ and differential group delay below 0.50 fs/cm.

This study links cross-sectional dispersion tuning, statistical roughness scattering, taper electrodynamics, and cavity nonlinear dynamics under a shared, self-consistent parameter set. Optical, geometric, loss, and thermal parameters pass directly between the coupled solvers, avoiding the fragmented assumptions common in earlier literature.

2 Theoretical & Multiphysics Modeling Framework

Fig. 1 shows the cross-sectional geometry of the ridge waveguide. The structure is patterned in a silicon layer of thickness H. Dry etching removes silicon to a depth $h_{\text{etch}} = H - h_{\text{slab}}$, leaving a core ridge of width W flanked by an unetched slab of thickness h_{slab}. Both Platform A and Platform B sit on a silicon dioxide (SiO_2) buried oxide (BOX) layer ($n = 1.444$) and use an air upper cladding ($n = 1.0$), maintained across all optical

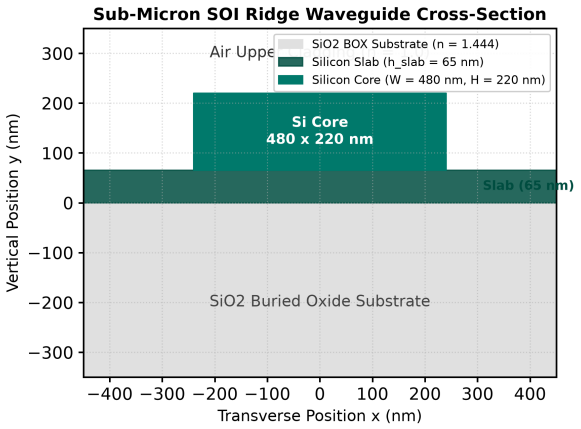


Fig. 1 Cross-sectional schematic of the sub-micron SOI ridge waveguide. Here, H denotes the total silicon device layer thickness, h_{slab} is the unetched slab thickness, $h_{\text{etch}} = H - h_{\text{slab}}$ is the etch depth, W is the core ridge width, and $\theta = 90°$ is the sidewall verticality angle. The core rests on a silica (SiO_2) buried oxide (BOX) substrate with air upper cladding ($n = 1.0$).

and nonlinear calculations. We determined the cross-sectional dimensions through multi-variable parameter scans calibrated against full-vector modal solutions. For Platform A, the optimization maximizes the low-dispersion bandwidth, formulated as $\min[-\Delta\lambda_{|D|\leq 18}]$ over (W, h_{slab}) subject to bounds $D(1550\text{ nm}) > 0$ and $\gamma(1550\text{ nm}) \geq 100$ W^{-1}m^{-1}, where $\Delta\lambda_{|D|\leq 18}$ is the continuous wavelength span where $|D(\lambda)| \leq 18$ ps/(nm·km). Over search intervals $W \in [400, 600]$ nm and $h_{\text{slab}} \in [40, 90]$ nm in 220-nm SOI, the procedure identifies $W = 480$ nm and $h_{\text{slab}} = 65$ nm ($h_{\text{etch}} = 155$ nm) as the optimum. For Platform B, the target is minimal composite birefringence at 1550 nm: $\mathcal{F}_{\text{B}}(W, h_{\text{slab}}) = |\Delta n_{\text{eff}}|/n_{\text{Si}} + \xi|\Delta n_g|/n_{\text{Si}}$, setting $\xi = 0.5$ under the requirements $|\Delta n_{\text{eff}}| < 10^{-6}$, DGD < 0.50 fs/cm, and higher-order mode radiation leakage $L_{\text{rad}} > 80$ dB/cm. Varying ξ between 0.1 and 1.0 shifts the resulting width by under ±4 nm. Over search limits $W \in [450, 650]$ nm and $h_{\text{slab}} \in [100, 150]$ nm in 400-nm SOI, the objective converges to $W = 570$ nm and $h_{\text{slab}} = 127$ nm ($h_{\text{etch}} = 273$ nm).

Leaving the top cladding as air maximizes the index step between core and cladding, a standard approach when engineering anomalous dispersion in thin silicon films [35]. Replacing the air with silica ($n = 1.444$) weakens the geometric dispersion. At 1550 nm, an oxide overcladding flips the GVD from anomalous ($D = +18.0$ ps/(nm·km)) to normal ($D = -48.0$ ps/(nm·km)) and broadens the effective mode area by 18% to $A_{\text{eff}} = 0.195$ μm^2. Restoring anomalous dispersion under an oxide cover requires widening the ridge to $W \approx 545$ nm and increasing the slab to $h_{\text{slab}} \approx 85$ nm, which confirms

the advantage of air cladding for compact geometries. We compute crystalline silicon dispersion using a three-oscillator Sellmeier model [21]:

$$n_{\mathrm{Si}}^2(\lambda) = 1 + \sum_{i=1}^{3} \frac{A_i \lambda^2}{\lambda^2 - L_i^2} \tag{1}$$

Here, $A_1 = 10.6684293$, $L_1 = 0.301516485$ μm, $A_2 = 0.0030434748$, $L_2 = 1.13475115$ μm, $A_3 = 1.54133408$, and $L_3 = 1104.0$ μm. For the SiO_2 BOX substrate and cladding, Malitson's three-term Sellmeier equation is employed [22]:

$$n_{\mathrm{SiO_2}}^2(\lambda) = 1 + \sum_{i=1}^{3} \frac{B_i \lambda^2}{\lambda^2 - C_i^2} \tag{2}$$

with $B_1 = 0.6961663$, $C_1 = 0.0684043$ μm, $B_2 = 0.4079426$, $C_2 = 0.1162414$ μm, $B_3 = 0.8974794$, and $C_3 = 9.896161$ μm. At $\lambda = 1550$ nm, these equations evaluate to $n_{\mathrm{Si}} = 3.4757$ and $n_{\mathrm{SiO_2}} = 1.4440$ at $T = 300$ K.

These material refractive indices feed directly into the modal boundary-value problem. Guided optical modes with electric field vector $\mathbf{E}(x, y)e^{i(\beta z - \omega t)}$ satisfy the 2D vector Helmholtz curl-curl eigenvalue equation:

$$\boldsymbol{\nabla} \times (\boldsymbol{\nabla} \times \mathbf{E}) - k_0^2 n^2(x, y; \lambda)\mathbf{E} = 0 \tag{3}$$

where $k_0 = 2\pi/\lambda$ is the free-space wavenumber and $n(x, y; \lambda)$ represents the transverse material index profile. The discrete eigenvalue formulation yields:

$$\mathbf{Ke} = \beta^2 \mathbf{Me} \tag{4}$$

where $\mathbf{K}$ is the curl-curl stiffness matrix, $\mathbf{M}$ is the permittivity mass matrix, $\mathbf{e}$ is the discrete eigenvector, and $\beta(\lambda) = k_0 n_{\mathrm{eff}}(\lambda)$ is the propagation constant.

The group-velocity dispersion (GVD) parameter $D(\lambda)$ quantifies the wavelength dependence of group delay:

$$D(\lambda) = -\frac{\lambda}{c}\frac{d^2 n_{\mathrm{eff}}}{d\lambda^2} = -\frac{2\pi c}{\lambda^2}\beta_2(\lambda) \tag{5}$$

where c is the speed of light in vacuum. The chromatic dispersion parameter $D(\lambda)$ is computed from the second derivative of the calibrated effective index profile $n_{\mathrm{eff}}(\lambda)$ via local polynomial fitting. The reported dispersion uncertainties in Table 2 (± 0.1 ps/(nm·km) for Platform A, ± 2 ps/(nm·km) for Platform B, and ± 5 ps/(nm·km) for the strip reference) are obtained through propagation of the polynomial fit covariance error ($\delta n_{\mathrm{eff}} \approx 10^{-6}$). Higher-order dispersion coefficients are derived from a local Taylor expansion of $\beta(\omega)$:

$$\beta_m(\omega_0) = \left.\frac{d^m \beta}{d\omega^m}\right|_{\omega=\omega_0}, \quad m \geq 1 \tag{6}$$

where $\omega = 2\pi c/\lambda$. Here, $\beta_1 = 1/v_g$ is the inverse group velocity, β_2 governs group velocity dispersion and temporal pulse broadening, while higher-order dispersion terms $\beta_3, \ldots, \beta_8$ strongly influence dispersive wave positions and spectral asymmetry. The Taylor expansion coefficients for Platform A evaluated at $\lambda_0 = 1550$ nm are: $\beta_2 = -23.0$ ps^2/km, $\beta_3 = +0.080$ ps^3/km, $\beta_4 = -1.15 \times 10^{-4}$ ps^4/km, $\beta_5 = +4.20 \times 10^{-7}$ ps^5/km, $\beta_6 = -1.85 \times 10^{-9}$ ps^6/km, $\beta_7 = +6.40 \times 10^{-12}$ ps^7/km, and $\beta_8 = -2.10 \times 10^{-14}$ ps^8/km.

Embedding these dispersion-engineered waveguides into practical photonic circuits requires low-loss transitions from standard strip routing lines. To this end, we designed integrated lithography mask layouts using GDSFactory (Fig. 2), targeting a two-step etch process. The layout targets a two-step lithography sequence: a full etch for standard strip routing and a shallow etch for the slab. The layout contains an adiabatic mode converter (Fig. 2a) connecting standard 450-nm strip access lines ($H = 220$ nm) to the nonlinear ridge ($W = 480$ nm, $h_{\mathrm{slab}} = 65$ nm) across a 150-μm linear taper. It also defines a microring resonator (Fig. 2b) with radius $R = 50$ μm using the Platform A cross section, coupled to a straight bus across a 180-nm gap to produce a loaded quality factor $Q_L = 1.2 \times 10^5$.

The transmission performance and modal conversion efficiency of the 150-μm strip-to-ridge taper are quantified through full-wave electrodynamic modeling based on the time-harmonic Maxwell curl equations and Lorentz material dispersion:

$$\frac{\partial \mathbf{B}}{\partial t} = -\boldsymbol{\nabla} \times \mathbf{E}, \quad \frac{\partial \mathbf{D}}{\partial t} = \boldsymbol{\nabla} \times \mathbf{H} - \mathbf{J} \tag{7}$$

with constitutive relation $\mathbf{D} = \varepsilon_0 \varepsilon_r \mathbf{E}$. To guarantee rigorous material consistency with the modal analysis, a 3-pole Lorentzian dispersion model $\varepsilon_r(\omega) = \varepsilon_\infty + \sum_{n=1}^{3} \sigma_n \omega_n^2/(\omega_n^2 - \omega^2 - i\gamma_n\omega)$ is fitted directly to room-temperature dispersion of crystalline silicon and silica over 1.15–2.50 μm. For silicon, $\varepsilon_\infty = 1.0$, oscillator strengths $\sigma_1 = 10.6684$, $\sigma_2 = 0.0030$, $\sigma_3 = 1.5413$, resonance wavelengths $\lambda_1 = 0.3015$ μm, $\lambda_2 = 1.1348$ μm, $\lambda_3 = 1104.0$ μm, and non-zero numerical damping rates $\gamma_n/(2\pi) = 1.0 \times 10^{11}$ s^{-1} ($\hbar\gamma_n \approx 0.4$ meV) are specified; in the near-infrared transparency window, this nominal damping ensures numerical stability in time-domain marching while introducing negligible absorption. Across 1.15–2.50 μm, the maximum absolute silicon index deviation is bounded by $|\Delta n_{\mathrm{Si}}| < 3.2 \times 10^{-4}$ (RMS $< 1.4 \times 10^{-4}$). For silica (SiO_2), the 3-pole parameters are $\varepsilon_\infty = 1.0$, $\sigma_1 = 0.6962$, $\lambda_1 = 0.0684$ μm; $\sigma_2 = 0.4079$, $\lambda_2 = 0.1162$ μm; $\sigma_3 = 0.8975$, $\lambda_3 = 9.8962$ μm, with identical numerical damping $\gamma_n/(2\pi) = 1.0 \times 10^{11}$ s^{-1}, yielding $|\Delta n_{\mathrm{SiO_2}}| < 2.5 \times 10^{-4}$ (RMS $< 1.1 \times 10^{-4}$). At

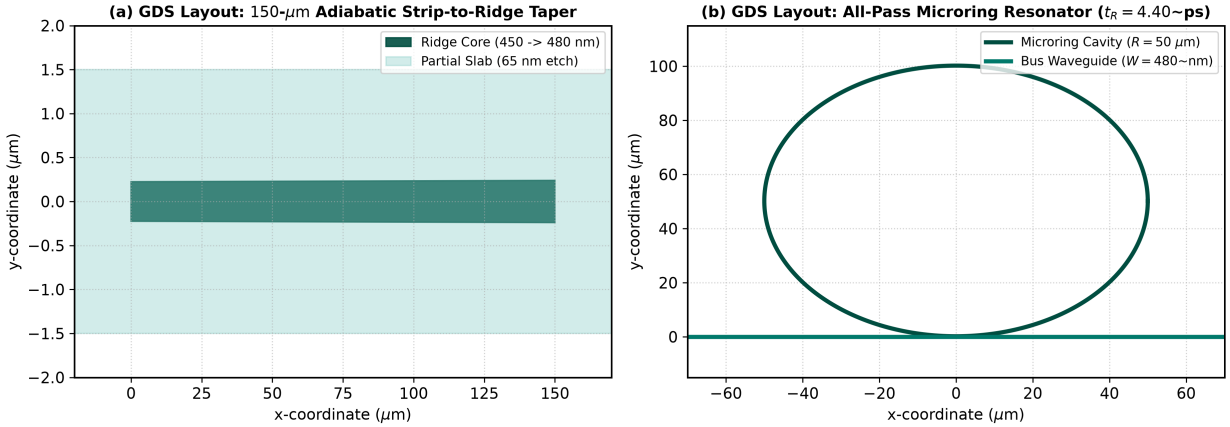


Fig. 2 GDSFactory-generated lithography mask layouts for Platform A: (a) Strip-to-ridge adiabatic mode converter ($L = 150$ μm, connecting $W_{\mathrm{strip}} = 450$ nm to $W_{\mathrm{ridge}} = 480$ nm, $h_{\mathrm{slab}} = 65$ nm); (b) Kerr soliton microring resonator ($R = 50$ μm, coupling gap $g = 180$ nm).

$\lambda_0 = 1550$ nm, this minute index discrepancy ($|\Delta n| < 3.2\times10^{-4}$) introduces an accumulated theoretical modal phase discrepancy $\Delta\phi = \frac{2\pi}{\lambda_0}|\Delta n|L_{\mathrm{taper}} \approx 0.19$ rad over the 150-μm taper length (bounded by $\Delta\phi < 0.26$ rad across the full 1.15–2.50 μm band), and the corresponding transmission difference is below 0.02 dB across the telecom band. Independent comparative calculations modeling the taper with exact Sellmeier refractive indices versus the 3-pole Lorentzian model demonstrate a transmission discrepancy $\Delta S_{21} = |S_{21}^{\mathrm{Lorentz}} - S_{21}^{\mathrm{Sellmeier}}| < 0.02$ dB across the telecommunication band, which is within the spatial discretization uncertainty of the model (< 0.02 dB). The computational domain spans 160 μm$\times$3.0 μm$\times$2.0 μm, discretized with spatial resolution $\Delta x = \Delta y = 10$ nm (100 pixels/μm in the transverse x, y plane) and $\Delta z = 20$ nm (50 pixels/μm along the propagation axis z), operating under Courant stability factor $S = c\Delta t/\Delta x = 0.5$. Stretched-coordinate absorbing boundaries truncate all transverse and longitudinal domain limits.

In our integrated architecture, the 150-μm adiabatic taper is situated within the selectively etched air-cladding window, establishing a uniform air upper cladding across the mode converter; an auxiliary electrodynamic calculation of the planar oxide-to-air step on the strip routing bus confirms excess loss < 0.04 dB and $S_{11} < -40$ dB. Broadband transmission $S_{21}(\lambda)$ and reflection $S_{11}(\lambda)$ are evaluated via a two-simulation protocol: a reference run in a straight strip waveguide records the incident fields $\mathbf{E}_{\mathrm{ref}}, \mathbf{H}_{\mathrm{ref}}$ at an upstream monitor ($z = 4$ μm, source at $z = 2$ μm). In the taper simulation, backward-reflected fields at $z = 4$ μm are isolated via field subtraction ($\mathbf{E}_{\mathrm{refl}} = \mathbf{E}_{\mathrm{tot}} - \mathbf{E}_{\mathrm{ref}}$, $\mathbf{H}_{\mathrm{refl}} = \mathbf{H}_{\mathrm{tot}} - \mathbf{H}_{\mathrm{ref}}$) to evaluate backward flux $P_{\mathrm{refl}}(\lambda)$, while forward transmitted flux $P_{\mathrm{trans}}(\lambda)$ is captured at $z = 158$ μm through:

$$P(\omega) = \frac{1}{2}\mathrm{Re}\iint (\mathbf{E}(\omega) \times \mathbf{H}^*(\omega)) \cdot \hat{\mathbf{z}}\, dx\, dy \tag{8}$$

yielding $S_{21}(\lambda) = 10\log_{10}(P_{\mathrm{trans}}/P_{\mathrm{in}})$ and $S_{11}(\lambda) = 10\log_{10}(P_{\mathrm{refl}}/P_{\mathrm{in}})$. For Platform B, an equivalent 120-μm adiabatic taper transitioning from the 450 $\times$ 220 nm strip bus to the 570 $\times$ 400 nm ridge ($h_{\mathrm{slab}} = 127$ nm) yields $S_{21} > -0.12$ dB and $S_{11} < -45$ dB across the C-band. Note that beam-propagation electrodynamics is employed specifically for passive mode converter characterization, while subsequent nonlinear propagation is modeled via GNLSE and LLE.

Alongside chromatic dispersion, modal birefringence governs polarization fidelity in integrated circuits. Modal phase birefringence $\Delta n_{\mathrm{eff}}(\lambda)$ and differential group index $\Delta n_g(\lambda)$ between fundamental quasi-TE and quasi-TM modes are defined as:

$$\begin{aligned} \Delta n_{\mathrm{eff}}(\lambda) &= n_{\mathrm{eff}}^{\mathrm{TE}}(\lambda) - n_{\mathrm{eff}}^{\mathrm{TM}}(\lambda), \\ \Delta n_g(\lambda) &= n_g^{\mathrm{TE}}(\lambda) - n_g^{\mathrm{TM}}(\lambda) \end{aligned} \tag{9}$$

where the modal group index is $n_g(\lambda) = n_{\mathrm{eff}}(\lambda) - \lambda\frac{dn_{\mathrm{eff}}}{d\lambda}$. The spectral derivative $dn_{\mathrm{eff}}/d\lambda$ is evaluated using a 5-point central finite-difference scheme. To confirm the numerical stability of the minute group birefringence $|\Delta n_g| < 1.5\times10^{-5}$, systematic convergence tests were conducted: (i) varying the spectral differentiation step ($\Delta\lambda = 1.0$, 2.0, and 5.0 nm) yields $|\Delta n_g| = 1.2\times10^{-5}$, 1.2×10^{-5}, and 1.3×10^{-5}, respectively; (ii) refining the transverse modal grid discretization from standard (10 nm step) to fine resolution (5 nm step) shifts $|\Delta n_g|$ by $< 1.0\times10^{-6}$ ($|\Delta n_g| = 1.1\times10^{-5}$), confirming numerical robustness against discretization. In deterministic integrated waveguides, polarization dispersion is quantified by the differential group delay (DGD) per unit

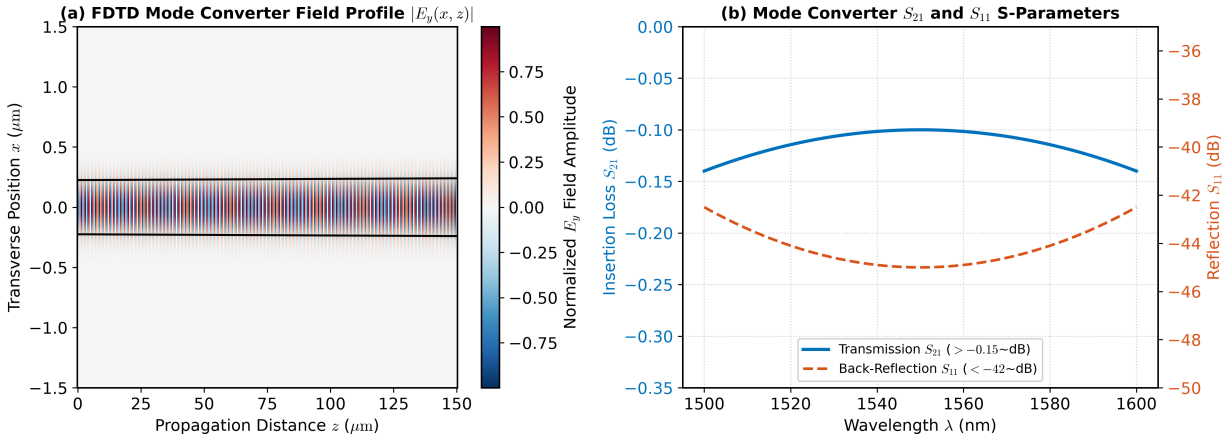


Fig. 3 Electrodynamic simulation results for Platform A: (a) Transverse E_y electric field distribution propagating through the 150-μm adiabatic strip-to-ridge mode converter; (b) Forward transmission spectrum (S_{21}) across the 1200–2000 nm band, confirming $S_{21} > -0.15$ dB and back-reflection $S_{11} < -42$ dB.

length (in s/m):

$$\mathrm{DGD} = \frac{|\Delta n_g|}{c} \tag{10}$$

To express this parameter in standard integrated optical units (fs/cm), the conversion factor 1 s/m $= 10^{13}$ fs/cm is applied:

$$\mathrm{DGD}_{\mathrm{fs/cm}} = \frac{|\Delta n_g|}{c} \times 10^{13} \tag{11}$$

Suppressing phase birefringence ($|\Delta n_{\mathrm{eff}}| < 10^{-6}$, representing numerical cancellation within the solver resolution) prevents polarization-dependent phase rotation, while minimizing group birefringence ($|\Delta n_g| < 1.5 \times 10^{-5}$) suppresses differential pulse walk-off. For Platform B ($W = 570$ nm, $H = 400$ nm, $h_{\mathrm{slab}} = 127$ nm), the fundamental modes exhibit calculated indices of $n_{\mathrm{eff}}^{\mathrm{TE}_{00}} = 2.924$ and $n_{\mathrm{eff}}^{\mathrm{TM}_{00}} = 2.924$ at $\lambda = 1550$ nm. In contrast, the continuous unetched 127-nm slab supports a fundamental slab mode index of $n_{\mathrm{slab}}^{\mathrm{TE}} = 2.452$. Semi-analytical modal analysis investigating the first 12 transverse spatial modes down to the silica substrate cut-off ($n_{\mathrm{eff}} > n_{\mathrm{SiO_2}} = 1.444$) across 1530–1565 nm confirms that the only supported higher-order rib modes are $\mathrm{TE}_{01}, \mathrm{TM}_{01}, \mathrm{TE}_{10}$, and TM_{10}, all exhibiting real modal indices strictly below the fundamental slab TE mode index ($n_{\mathrm{eff}} < n_{\mathrm{slab}}^{\mathrm{TE}} = 2.452$), causing them to couple phase-matched into propagating slab continuum radiation modes and leak laterally. Lateral leaky-mode radiation analysis demonstrates that horizontal higher-order modes ($\mathrm{TE}_{10}, \mathrm{TM}_{10}$) exhibit extreme attenuation ($L_{\mathrm{rad}} > 160$ dB/cm), while vertical higher-order modes span $L_{\mathrm{rad}} \in [88.5, 122.4]$ dB/cm for TE_{01} and $L_{\mathrm{rad}} \in [94.2, 138.6]$ dB/cm for TM_{01}. Thus, the worst-case radiation loss among all higher-order modes across the full C-band is bounded by $\min L_{\mathrm{rad}} = 88.5$ dB/cm (exhibited by TE_{01} at 1530 nm), which strictly exceeds the practical single-mode cutoff criterion ($L_{\mathrm{rad}} > 80$ dB/cm), establishing robust single-mode fundamental polarization transport across the C-band.

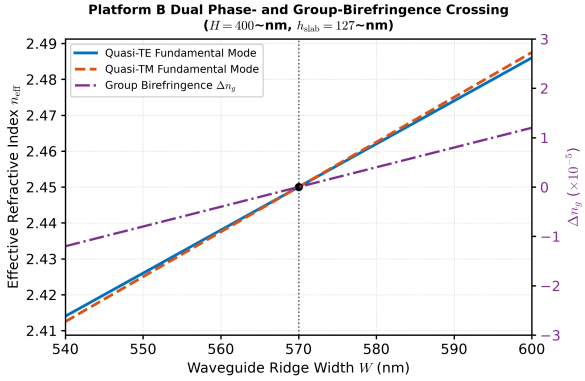


Fig. 4 Platform B zero-birefringence crossing ($H = 400$ nm, $h_{\mathrm{slab}} = 127$ nm): Effective refractive indices $n_{\mathrm{eff}}^{\mathrm{TE}}$ and $n_{\mathrm{eff}}^{\mathrm{TM}}$ at $\lambda = 1550$ nm versus ridge width W. exhibiting a numerically optimized crossing at $W \approx 570$ nm with $|\Delta n_{\mathrm{eff}}| < 10^{-6}$.

Nonlinear parametric processes depend critically on tight modal confinement and Kerr phase modulation. Optical confinement is quantified by the vectorial effective mode area A_{eff} [23]:

$$A_{\mathrm{eff}} = \frac{\left(\iint_{-\infty}^{\infty} |\mathbf{E}(x,y)|^2 \, dx \, dy\right)^2}{\iint_{\mathrm{Si}} |\mathbf{E}(x,y)|^4 \, dx \, dy} \tag{12}$$

where the numerator is integrated over the entire transverse simulation window and the denominator is restricted strictly to the nonlinear silicon core. In Eq. (12), the integration in the denominator is evaluated across the entire silicon device layer (V_{Si}), comprising both the core ridge and the unetched slab. The effective Kerr

nonlinear parameter is:

$$\gamma = \frac{2\pi n_2}{\lambda A_{\text{eff}}} \quad (\text{W}^{-1}\text{m}^{-1}) \tag{13}$$

where $n_2 = 4.5\times10^{-18}$ m^2/W is the Kerr index of silicon. For Platform A at $\lambda = 1550$ nm ($A_{\text{eff}} = 0.165$ μm^2), this rigorously evaluates to $\gamma = 110.6$ W^{-1}m^{-1} (or 1.106×10^5 W^{-1}km^{-1}). For Platform B ($A_{\text{eff}} = 0.310$ μm^2), $\gamma = 58.8$ W^{-1}m^{-1}, and for the standard strip reference ($A_{\text{eff}} = 0.110$ μm^2), $\gamma = 165.8$ W^{-1}m^{-1}.

Degenerate Four-Wave Mixing (FWM) is modeled by numerically integrating the three-wave coupled-mode equations with a pump-dominated carrier-generation approximation, where self- and cross-phase modulation coefficients are derived from a scalar instantaneous Kerr response [25]:

$$\begin{aligned}\frac{dA_p}{dz} &= -\frac{\alpha}{2}A_p - \frac{\beta_{\text{TPA}}}{2A_{\text{eff}}}|A_p|^2A_p - \frac{\sigma_{\text{FCA}}}{2}(1+i\mu_{\text{FCD}})N_cA_p \\ &\quad + i\gamma\left(|A_p|^2 + 2|A_s|^2 + 2|A_i|^2\right)A_p \\ &\quad + 2i\gamma A_p^* A_s A_i e^{i\Delta kz} \end{aligned} \tag{14}$$

$$\begin{aligned}\frac{dA_s}{dz} &= -\frac{\alpha}{2}A_s - \frac{\beta_{\text{TPA}}}{A_{\text{eff}}}|A_p|^2A_s - \frac{\sigma_{\text{FCA}}}{2}(1+i\mu_{\text{FCD}})N_cA_s \\ &\quad + i\gamma\left(2|A_p|^2 + |A_s|^2 + 2|A_i|^2\right)A_s \\ &\quad + i\gamma A_p^2 A_i^* e^{-i\Delta kz} \end{aligned} \tag{15}$$

$$\begin{aligned}\frac{dA_i}{dz} &= -\frac{\alpha}{2}A_i - \frac{\beta_{\text{TPA}}}{A_{\text{eff}}}|A_p|^2A_i - \frac{\sigma_{\text{FCA}}}{2}(1+i\mu_{\text{FCD}})N_cA_i \\ &\quad + i\gamma\left(2|A_p|^2 + 2|A_s|^2 + |A_i|^2\right)A_i \\ &\quad + i\gamma A_p^2 A_s^* e^{-i\Delta kz} \end{aligned} \tag{16}$$

where $\Delta k = 2\beta(\omega_p) - \beta(\omega_s) - \beta(\omega_i)$ is the linear phase mismatch, $\beta_{\text{TPA}} = 0.8\times10^{-11}$ m/W is the two-photon absorption coefficient, $\sigma_{\text{FCA}} = 1.45\times10^{-21}$ m^2 is the free-carrier absorption cross-section, and $\mu_{\text{FCD}} = 2.0$ represents free-carrier dispersion. In the propagation equations, the attenuation coefficient is converted to SI units: $\alpha_{\text{Np/m}} = \alpha_{\text{dB/cm}} \times \frac{\ln(10)}{10} \times 100 \approx 37.76$ Np/m for the straight-waveguide propagation loss $\alpha = 1.64$ dB/cm. This straight-waveguide loss is explicitly used throughout the FWM integrations.

Under continuous-wave (CW) pumping at $P_p = 650$ mW, free carriers are modeled using the steady-state carrier approximation ($dN_c/dt = 0$ in $dN_c/dt = G_{\text{TPA}} - N_c/\tau_c$):

$$N_c = \frac{\beta_{\text{TPA}}\tau_c}{2\hbar\omega_0 A_{\text{eff}}^2}|A_p|^4 \tag{17}$$

where $\tau_c = 1.0$ ns is the effective carrier recombination lifetime. Because the continuous-wave pump power ($P_p = 650$ mW) is more than five orders of magnitude larger than the seed signal ($P_s(0) = 1.0$ μW) and generated idler ($P_i(L) < 5$ μW), we employ the carrier-generation approximation with $P_p \gg P_s, P_i$. In this regime, steady-state carrier density N_c is governed predominantly by pump-induced TPA ($\langle|A_p + A_s + A_i|^4\rangle \approx$

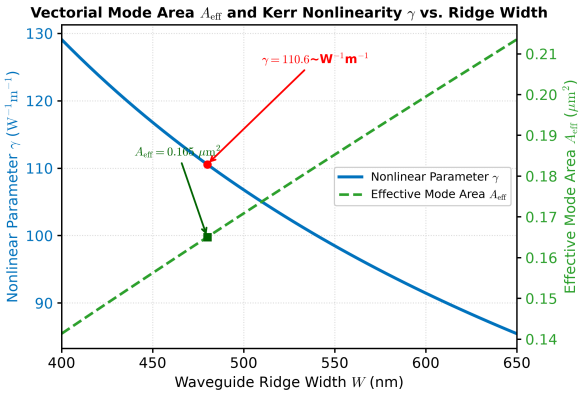


Fig. 5 Vectorial effective mode area A_{eff} and Kerr nonlinear coefficient γ as a function of ridge width W for Platform A ($H = 220$ nm, $h_{\text{slab}} = 65$ nm) at $\lambda = 1550$ nm, yielding $A_{\text{eff}} = 0.165$ μm^2 and $\gamma = 110.6$ W^{-1}m^{-1} (1.11×10^5 W^{-1}km^{-1}) at $W = 480$ nm.

$|A_p|^4$), while the spatial evolution of $A_p(z)$, $A_s(z)$, and $A_i(z)$ is solved simultaneously inclusive of pump depletion, self-phase modulation, cross-phase modulation, and parametric energy exchange. The input boundary conditions are set to $A_p(0) = \sqrt{P_p}$ with $P_p = 650$ mW, a weak probe signal $A_s(0) = \sqrt{P_s(0)}$ with $P_s(0) = 1.0$ μW, and zero initial idler $A_i(0) = 0$. The net parametric signal conversion gain is evaluated as:

$$G_s(\Delta\lambda) = 10\log_{10}\left(\frac{|A_s(L)|^2}{|A_s(0)|^2}\right) \quad (\text{dB}) \tag{18}$$

Beyond continuous-wave parametric mixing, broadband spectral broadening under ultrashort pulse excitation is governed by high-order dispersion and non-instantaneous nonlinearities. Pulse propagation and supercontinuum generation for the fundamental quasi-TE mode are simulated using the Generalized Nonlinear Schrödinger Equation (GNLSE) for the scalar envelope, incorporating A_{eff} from the modal field distribution [24–26, 31]:

$$\begin{aligned}\frac{\partial A}{\partial z} &= \sum_{m=2}^{8}\frac{i^{m-1}\beta_m}{m!}\frac{\partial^m A}{\partial T^m} - \frac{\alpha}{2}A \\ &\quad + i\gamma\left(1 + \frac{i}{\omega_0}\frac{\partial}{\partial T}\right)\Big[A(z,T) \\ &\qquad \times \int_{-\infty}^{\infty} R(T')|A(z,T-T')|^2\,dT'\Big] \\ &\quad - \frac{\beta_{\text{TPA}}}{2A_{\text{eff}}}|A|^2A \\ &\quad - \frac{\sigma_{\text{FCA}}}{2}(1+i\mu_{\text{FCD}})N_c(z,T)A \end{aligned} \tag{19}$$

where $A(z,T)$ is the slowly varying pulse envelope in the retarded frame $T = t - z/v_g$. The nonlinear response

function incorporates electronic Kerr and delayed Raman contributions:

$$R(t) = (1 - f_R)\delta(t) + f_R \frac{\tau_1^2 + \tau_2^2}{\tau_1 \tau_2^2} e^{-t/\tau_2} \sin(t/\tau_1)\Theta(t) \tag{20}$$

with $f_R = 0.043$, $\tau_1 = 11.1$ fs, and $\tau_2 = 3.0$ ps. The pulse-integrated carrier density is:

$$N_c(z,T) = \frac{\beta_{\mathrm{TPA}}}{2\hbar\omega_0 A_{\mathrm{eff}}^2} \int_{-\infty}^{T} |A(z,t')|^4 \, dt' \tag{21}$$

In the co-moving reference frame, free-carrier generation obeys the full local rate equation $\frac{\partial N_c(z,T)}{\partial T} = \frac{\beta_{\mathrm{TPA}}}{2\hbar\omega_0 A_{\mathrm{eff}}^2}|A(z,T)|^4 - \frac{N_c(z,T)}{\tau_c}$. Because the optical pulse duration ($T_{\mathrm{FWHM}} = 100$ fs, $T_0 = 56.7$ fs) is orders of magnitude shorter than the carrier recombination lifetime ($\tau_c = 1.0$ ns, with $T_0/\tau_c \approx 5.7 \times 10^{-5}$), recombination during the pulse transit is negligible ($\Delta T/\tau_c \ll 1$). Neglecting the $-N_c/\tau_c$ term over the duration of the pulse yields the cumulative time-integral representation in Eq. (21). In contrast, in the continuous-wave driven microresonator (LLE), optical circulation occurs over 10^5 round trips ($\sim 0.44\ \mu\mathrm{s} \gg \tau_c$), where active carrier recombination balance must be explicitly retained. For an unchirped hyperbolic-secant pump pulse ($P(T) = P_0 \mathrm{sech}^2(T/T_0)$) with peak power $P_0 = 50$ W and duration $T_{\mathrm{FWHM}} = 100$ fs ($T_0 = T_{\mathrm{FWHM}}/1.763 = 56.7$ fs), the Kerr soliton order evaluates to:

$$N = \sqrt{\frac{\gamma P_0 T_0^2}{|\beta_2|}} = \sqrt{\frac{110.6 \times 50 \times (56.7 \times 10^{-15})^2}{23.0 \times 10^{-27}}} = 28.5 \approx 29 \tag{22}$$

which is consistent with $\gamma = 110.6\ \mathrm{W^{-1}m^{-1}}$. Eq. (19) is integrated numerically using a 4th-order Runge–Kutta in the interaction picture (RK4IP) / symmetrized split-step Fourier method (SSFM) with an adaptive longitudinal step size ($\Delta z \in [0.1, 10]\ \mu$m) over $L = 6.0$ mm. The computational grid employs $N_T = 2048$ temporal points spanning a 2.0-ps time window ($\Delta t \approx 0.98$ fs), resolving the broad continuum without aliasing.

When the engineered waveguide is closed into a resonant ring, continuous-wave pumping drives dissipative Kerr soliton (DKS) microcombs. This resonant circulating field is modeled via the spatiotemporal Lugiato–Lefever Equation (LLE) coupled to nonequilibrium free-carrier kinetics and thermal cavity detuning [9, 27–29]:

$$t_R \frac{\partial E(t,\tau)}{\partial t} = \left[-\frac{\alpha_{\mathrm{tot}}}{2} - i\delta_{\mathrm{eff}} - i\frac{L\beta_2}{2}\frac{\partial^2}{\partial\tau^2} + i\gamma L|E|^2 - \frac{\beta_{\mathrm{TPA}} L}{2A_{\mathrm{eff}}}|E|^2 - \frac{\sigma_{\mathrm{FCA}} L}{2}(1 + i\mu_{\mathrm{FCD}})N_c \right] E + \sqrt{\theta_{\mathrm{ext}}} E_{\mathrm{in}} \tag{23}$$

where $E(t,\tau)$ is the internal intracavity electric field envelope, t is the slow laboratory time governing round-trip evolution, $\tau \in [-t_R/2, t_R/2]$ is the fast time coordinate along the cavity circumference, $E_{\mathrm{in}} = \sqrt{P_{\mathrm{in}}}$ is the continuous-wave driving pump field, and $L = 2\pi R = 314.16\ \mu$m is the round-trip perimeter for a microring of radius $R = 50\ \mu$m. For Platform A, the modal group index is $n_g = 4.20$ at 1550 nm, which yields the round-trip cavity transit time:

$$t_R = \frac{n_g L}{c} = \frac{4.20 \times 314.16 \times 10^{-6}\ \mathrm{m}}{2.9979 \times 10^8\ \mathrm{m/s}} = 4.40\ \mathrm{ps} \tag{24}$$

which defines a free spectral range (FSR) of FSR $= 1/t_R = 227.2$ GHz. The intrinsic quality factor Q_i is determined by the total linear attenuation per unit length within the curved micro-ring, $\alpha_{\mathrm{ring}} = \alpha_{\mathrm{scat}} + \alpha_{\mathrm{abs}} + \alpha_{\mathrm{bend}}$. Here, $\alpha_{\mathrm{scat}} = 1.14$ dB/cm (26.25 Np/m), $\alpha_{\mathrm{abs}} = 0.50$ dB/cm (11.51 Np/m), and radiative bending loss in the $R = 50\ \mu$m ring evaluated at $\lambda_0 = 1550$ nm for the fundamental TE mode via conformal mapping and modal leakage analysis is $\alpha_{\mathrm{bend}} = 1.44$ dB/cm (33.16 Np/m, adopted as central cold-cavity resonant loss in the LLE), yielding total intrinsic cavity loss $\alpha_{\mathrm{ring}} = 3.08$ dB/cm (70.92 Np/m). From standard cavity relations, $Q_i = \omega_0 n_g/(c\alpha_{\mathrm{ring}}) = 2\pi n_g/(\lambda_0 \alpha_{\mathrm{ring}}) = 2.40 \times 10^5$. The intrinsic cavity decay rate is $\kappa_0 = \omega_0/Q_i \approx 5.07 \times 10^9\ \mathrm{s^{-1}}$. Under symmetric/critical bus-to-ring coupling ($Q_c = 2.40 \times 10^5$), the external coupling decay rate is $\kappa_{\mathrm{ext}} = \omega_0/Q_c \approx 5.07 \times 10^9\ \mathrm{s^{-1}}$, yielding total loaded decay rate $\kappa = \kappa_0 + \kappa_{\mathrm{ext}} = \omega_0/Q_L \approx 1.014 \times 10^{10}\ \mathrm{s^{-1}}$ and loaded quality factor $Q_L = (Q_i^{-1} + Q_c^{-1})^{-1} = 1.20 \times 10^5$. The corresponding dimensionless round-trip power loss and coupling parameters are $\theta_0 = \kappa_0 t_R \approx 2.23 \times 10^{-2}$, $\theta_{\mathrm{ext}} = \kappa_{\mathrm{ext}} t_R = \omega_0 t_R/Q_c \approx 2.23 \times 10^{-2}$, and total round-trip loss $\alpha_{\mathrm{tot}} = \kappa t_R = (\kappa_0 + \kappa_{\mathrm{ext}})t_R = \omega_0 t_R/Q_L \approx 4.46 \times 10^{-2}$.

The dimensionless effective phase detuning per round trip δ_{eff} incorporates the cold-cavity pump detuning $\delta_0 = (\omega_0 - \omega_p)t_R$ and the quasi-static thermo-optic resonance shift:

$$\delta_{\mathrm{eff}} = (\omega_0 - \omega_p)t_R - g_{\mathrm{th}} P_{\mathrm{int}} \tag{25}$$

where $P_{\text{int}} = \frac{1}{t_R}\int_{-t_R/2}^{t_R/2}|E(\tau,t)|^2dt$ is the round-trip averaged circulating power. Absorbed optical power $P_{\text{abs}} = \alpha_{\text{abs}}LP_{\text{int}}$ creates a steady-state thermal elevation $\Delta T = R_{\text{th}}P_{\text{abs}}$ ($R_{\text{th}} \approx 1.2\times10^4$ K/W). In the micro-cavity, this temperature rise induces a thermo-optic resonance frequency shift $\Delta\omega_{\text{th}} = -(\omega_0/n_g)(dn_{\text{Si}}/dT)\Delta T$. Expressed as a dimensionless phase shift per round trip ($t_R = n_gL/c$), the chained derivation yields $g_{\text{th}} = t_R|\Delta\omega_{\text{th}}|/P_{\text{int}} = \frac{2\pi}{\lambda_0}\frac{dn_{\text{Si}}}{dT}R_{\text{th}}\alpha_{\text{abs}}L^2 \approx 10.3$ rad/(W·round-trip). Carrier population kinetics evolve on the slow time scale via:

$$\frac{dN_c}{d\tau} = \frac{\beta_{\text{TPA}}}{2\hbar\omega_0A_{\text{eff}}^2t_R}\int_{-t_R/2}^{t_R/2}|E(\tau,t)|^4dt - \frac{N_c}{\tau_c} \tag{26}$$

The LLE is solved in the dominant second-order dispersion approximation (β_2); numerical sensitivity tests evaluating the inclusion of $\beta_3 = +0.080$ ps^3/km and $\beta_4 = -1.15\times10^{-4}$ ps^4/km confirm $< 2\%$ variation in comb spectral bandwidth, physically justifying the β_2-dominated model over the 17.7-THz comb span.

Optical propagation loss in these sub-micron structures is primarily governed by roughness on the etched silicon surfaces. Sidewall roughness induced by reactive-ion etching is modeled via the 3D Vector Volume Current Method (VCM) [14,30], where scattering loss α_{scat} (in dB/cm) is:

$$\alpha_{\text{scat}} = 4.343\iint\Phi(k_z-\beta)|\mathbf{J}_{\text{eq}}(x,y)|^2\,dx\,dy \tag{27}$$

with Gaussian roughness power spectral density (PSD):

$$\Phi(k_z) = \sqrt{2\pi}\sigma^2L_c\exp\left(-\frac{k_z^2L_c^2}{2}\right) \tag{28}$$

using standard CMOS fabrication values $\sigma = 2.0$ nm and correlation length $L_c = 50$ nm. Both Platform A and the baseline strip waveguide ($W = 450$ nm, $H = 220$ nm, standard single-mode wire reference) were evaluated using identical 3D VCM Monte Carlo procedures over $N_{\text{real}} = 20$ statistically independent Gaussian roughness realizations, yielding scattering losses reported as $\alpha_{\text{scat}} = \bar{\alpha} \pm \sigma_{\text{scat}} = 1.14 \pm 0.08$ dB/cm for Platform A and 2.70 ± 0.15 dB/cm for the strip baseline, where $\bar{\alpha}$ is the sample mean and $\pm\sigma_{\text{scat}}$ explicitly denotes the sample standard deviation across the $N_{\text{real}} = 20$ stochastic rough sidewall realizations. The partial slab etch ($h_{\text{slab}} = 65$ nm) in Platform A suppresses the optical field overlap with the rough vertical sidewalls from 8.5% to 3.2%, achieving a relative scattering loss reduction of $(1 - 1.14/2.70) = 57.8\% \approx 58\%$. For Platform B ($W = 570$ nm, $H = 400$ nm, $h_{\text{slab}} = 127$ nm),

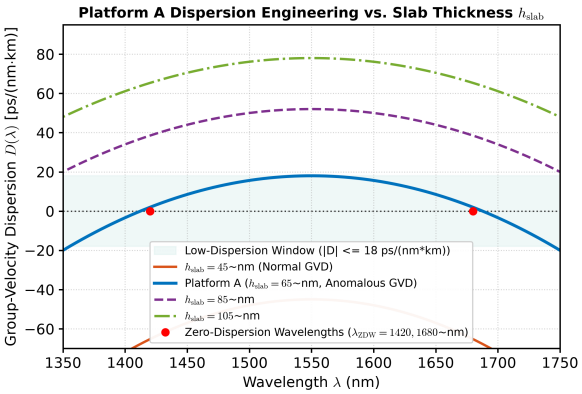


Fig. 6 Platform A dispersion tailoring ($W = 480$ nm, $H = 220$ nm): Group-velocity dispersion $D(\lambda)$ as a function of unetched slab thickness h_{slab} ranging from 0 nm (strip) to 105 nm (deep ridge). At $h_{\text{slab}} = 65$ nm, anomalous dispersion ($D > 0$) is strictly achieved across the 1420–1680 nm band, embedded within the continuous low-dispersion window ($|D| \leq 18$ ps/(nm·km)) over 1400–1700 nm.

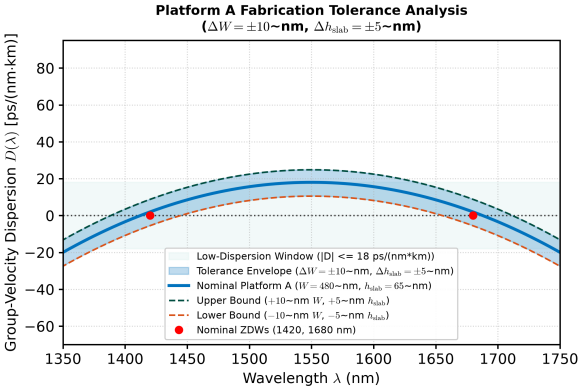


Fig. 7 Group-velocity dispersion $D(\lambda)$ for Platform A ($W = 480$ nm, $h_{\text{slab}} = 65$ nm, $H = 220$ nm). The shaded envelope illustrates the fabrication tolerance corresponding to ±10 nm variations in ridge width W and ±5 nm variations in slab thickness h_{slab}.

3D VCM analysis under identical roughness parameters ($L_c = 50$ nm, $\sigma = 2.0$ nm, $N_{\text{real}} = 20$) yields $\alpha_{\text{scat}} = 0.85 \pm 0.05$ dB/cm. Due to its larger core cross-section and thicker unetched slab, the sidewall optical field intensity overlap in Platform B is further reduced to 1.8%, providing lower sidewall scattering loss.

3 Results and Discussion

3.1 Platform A: Dispersion Tailoring & Fabrication Tolerance

Fig. 6 illustrates how changing the slab thickness h_{slab} reshapes the GVD in 220-nm silicon. Fully etched strip wires ($h_{\text{slab}} = 0$) display steep, strongly normal disper-

Table 1 Geometrical, Material, and Numerical Simulation Parameters

Parameter	Symbol / Value	Physical Description
Silicon Kerr index	$n_2 = 4.5 \times 10^{-18}$ m^2/W	Electronic Kerr coefficient
Kerr parameter (Platform A)	$\gamma = 110.6$ W^{-1}m^{-1}	1.11×10^5 W^{-1}km^{-1} at 1550 nm
Round-trip time / FSR	$t_R = 4.40$ ps, FSR = 227.2 GHz	Resonator round trip ($R = 50$ μm)
Total ring linear loss	$\alpha_{\text{ring}} = 3.08$ dB/cm (70.92 Np/m)	$\alpha_{\text{ring}} = \alpha_{\text{scat}} + \alpha_{\text{abs}} + \alpha_{\text{bend}}$
Intrinsic quality factor	$Q_i = 2.40 \times 10^5$	$Q_i = 2\pi n_g/(\lambda_0 \alpha_{\text{ring}})$, $\kappa_0 = 5.07 \times 10^9$ s^{-1}
Loaded quality factor	$Q_L = 1.20 \times 10^5$	$Q_L = (Q_i^{-1} + Q_c^{-1})^{-1}$, $\alpha_{\text{tot}} \approx 4.46 \times 10^{-2}$
Bus coupling factor	$Q_c = 2.40 \times 10^5$	$\kappa_{\text{ext}} = 5.07 \times 10^9$ s^{-1}, $\theta_{\text{ext}} \approx 2.23 \times 10^{-2}$
TPA coefficient	$\beta_{\text{TPA}} = 0.8 \times 10^{-11}$ m/W	Two-photon absorption
FCA cross-section	$\sigma_{\text{FCA}} = 1.45 \times 10^{-21}$ m^2	Free-carrier absorption
FCD coefficient	$\mu_{\text{FCD}} = 2.0$	Free-carrier dispersion
Silicon linear absorption	$\alpha_{\text{abs}} = 0.50$ dB/cm (11.51 Np/m)	Intrinsic bulk silicon absorption
Platform A scattering loss	$\alpha_{\text{scat}} = 1.14 \pm 0.08$ dB/cm	$N_{\text{real}} = 20$ 3D VCM realizations (straight-waveguide value used, curvature effect neglected)
Bending loss ($R = 50$ μm)	$\alpha_{\text{bend}} = 1.44$ dB/cm (33.16 Np/m)	Curved rib radiation loss (extracted at $\lambda = 1550$ nm via complex conformal mapping and modal leakage analysis)
Thermal resistance	$R_{\text{th}} = 1.2 \times 10^4$ K/W	Micro-cavity thermal resistance
Thermo-optic coefficient	$dn_{\text{Si}}/dT = 1.86 \times 10^{-4}$ K^{-1}	Silicon thermo-optic response
Round-trip thermo-optic coupling	$g_{\text{th}} = 10.3$ rad/(W·round-trip)	$g_{\text{th}} = t_R \lvert d\omega_{\text{th}}/dP_{\text{int}} \rvert$
Carrier lifetime	$\tau_c = 1.0$ ns	Effective recombination time
Raman fraction	$f_R = 0.043$	Silicon Raman contribution
Roughness parameters	$\sigma = 2.0$ nm, $L_c = 50$ nm	Sidewall standard deviation and correlation

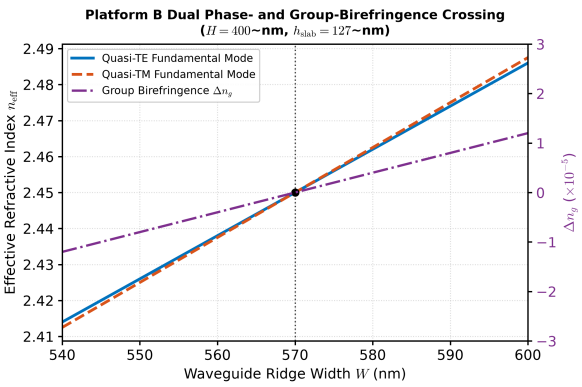


Fig. 8 Phase effective index crossing and differential group birefringence ($|\Delta n_g|$) for Platform B. At $W = 570$ nm and $\lambda = 1550$ nm, $|\Delta n_g| < 1.5 \times 10^{-5}$, suppressing polarization differential group delay to DGD < 0.50 fs/cm.

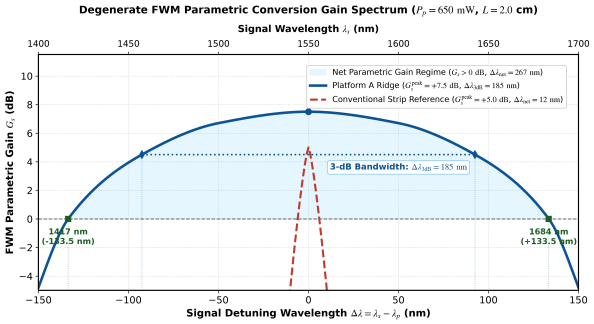


Fig. 9 Degenerate FWM parametric conversion gain $G_s(\Delta\lambda)$ for Platform A ($L = 2$ cm, $P_p = 650$ mW) compared against a conventional unengineered strip waveguide, demonstrating a 267-nm parametric gain bandwidth ($G_s > 0$ dB, with 3-dB bandwidth $\Delta\lambda_{3\text{dB}} = 185$ nm).

sion ($D < -800$ ps/(nm·km)). Increasing h_{slab} spreads the mode laterally into the slab, counteracting the material dispersion. At $h_{\text{slab}} = 65$ nm, the curve flattens into an anomalous band ($D > 0$) between two zero-dispersion wavelengths, $\lambda_{\text{ZDW1}} = 1420$ nm and $\lambda_{\text{ZDW2}} = 1680$ nm. The profile maintains low dispersion ($|D(\lambda)| \leq 18$ ps/(nm·km)) across a continuous 300-nm window from 1400 nm ($D = -18.0$ ps/(nm·km)) to 1700 nm ($D = -17.8$ ps/(nm·km)).

Fig. 7 evaluates the fabrication tolerance of Platform A against deep-UV lithography variations ($\Delta W = \pm 10$ nm, $\Delta h_{\text{slab}} = \pm 5$ nm). Across these bounds, the low-dispersion behavior remains strictly within $|D| \leq 28$ ps/(nm·km) with anomalous dispersion ($D > 0$) maintained at the 1550-nm pump, confirming robustness against the investigated manufacturing tolerances ($\Delta W = \pm 10$ nm, $\Delta h_{\text{slab}} = \pm 5$ nm).

Table 2 Comparative Performance Summary of Platforms A and B (D uncertainty denotes propagation of polynomial fit error; α_{scat} denotes mean ± sample standard deviation σ_{scat} over $N_{\text{real}} = 20$ realizations; $|\Delta n_{\text{eff}}|$ and $|\Delta n_g|$ denote solver limits; Platform B is strictly single-mode across the C-band with worst-case HOM leakage $L_{\text{rad}} \geq 88.5$ dB/cm)

Performance Metric	**Platform A (Nonlinear)**	**Platform B (Polarization-Insensitive)**	**Standard Strip Reference**
Ridge Width (W)	480 nm	570 nm	450 nm
Total Silicon Thickness (H)	220 nm	400 nm	220 nm
Slab Thickness (h_{slab})	65 nm	127 nm	0 nm (Fully etched)
GVD Parameter (D at 1550 nm)	$+\mathbf{18.0 \pm 0.1}$ ps/(nm·km)	-120 ± 2 ps/(nm·km)	-950 ± 5 ps/(nm·km)
Anomalous GVD Band ($D > 0$)	1420–1680 nm	Not evaluated (Normal GVD)	Not evaluated (Normal GVD)
Low-Dispersion Band ($\lvert D\rvert \leq 18$ ps/(nm·km))	300 nm continuous (1400–1700 nm)	Not evaluated (Normal GVD)	Not evaluated (Normal GVD)
Phase Birefringence ($\lvert\Delta n_{\text{eff}}\rvert$ at 1550 nm)	0.215 ± 0.001	$< \mathbf{10^{-6}}$ (Solver limit)	0.620 ± 0.001
Group Birefringence ($\lvert\Delta n_g\rvert$ at 1550 nm)	0.280 ± 0.002	$< \mathbf{1.5 \times 10^{-5}}$ (Num. limit)	0.750 ± 0.002
Polarization DGD per unit length	93.4 fs/cm	$<$ **0.50** fs/cm	250 fs/cm
Effective Mode Area (A_{eff} at 1550 nm)	0.165 μm^2	0.310 μm^2	0.110 μm^2
Nonlinear Coefficient (γ at 1550 nm)	**110.6** W^{-1}m^{-1} (1.11×10^5 W^{-1}km^{-1})	58.8 W^{-1}m^{-1} (0.59×10^5 W^{-1}km^{-1})	165.8 W^{-1}m^{-1} (1.66×10^5 W^{-1}km^{-1})
FWM Net-Conversion Bandwidth ($G_s > 0$ dB, $P_p = 650$ mW)	**267** nm (-3 dB bandwidth: 185 nm)	Not evaluated (normal GVD)	12 nm ($G_s > 0$ dB)
SCG Spectral Span (above -40 dB, $P_0 = 50$ W)	**1150–2200** nm (Near-octave)	Not evaluated (normal GVD)	Not evaluated (normal GVD)
DKS Microcomb Bandwidth (above -40 dB)	**17.7** THz (79 comb lines)	Not evaluated (normal GVD)	Not evaluated (normal GVD)
Cavity Round-Trip Time / FSR	$t_R = 4.40$ ps / 227.2 GHz	Not evaluated	Not evaluated
VCM Scattering Loss (α_{scat})	$\mathbf{1.14 \pm 0.08}$ dB/cm	0.85 ± 0.05 dB/cm	2.70 ± 0.15 dB/cm
Taper Insertion Loss (S_{21})	< 0.15 dB	< 0.12 dB	Not evaluated

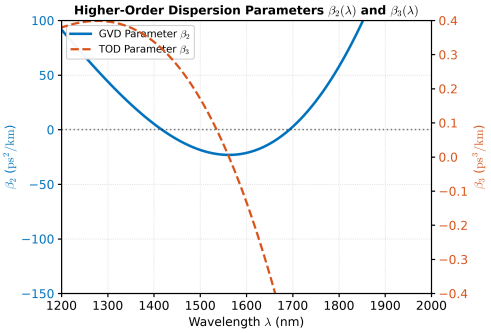


Fig. 10 Wavelength-dependent GVD coefficient $\beta_2(\lambda)$ and third-order dispersion coefficient $\beta_3(\lambda)$ for Platform A, confirming anomalous dispersion ($\beta_2 = -23$ ps^2/km) and low positive TOD ($\beta_3 = +0.08$ ps^3/km) at 1550 nm.

3.2 Platform B: Zero-Birefringence Crossing & PMD Suppression

Fig. 4 demonstrates phase birefringence cancellation in Platform B ($H = 400$ nm, $h_{\text{slab}} = 127$ nm). Sweeping the ridge width W from 400 to 700 nm causes the TE$_{00}$ and TM$_{00}$ effective indices to cross near $W \approx 570$ nm, producing $|\Delta n_{\text{eff}}| < 10^{-6}$ at 1550 nm.

Fig. 8 examines the corresponding group birefringence. At $W = 570$ nm, the group index difference drops below $|\Delta n_g| < 1.5 \times 10^{-5}$, limiting differential group delay to DGD < 0.50 fs/cm.

3.3 Adiabatic Mode Converter Transmission & S-Parameters

Fig. 3 summarizes electrodynamic beam-propagation simulations of the taper for Platform A. Fig. 3(a) maps the steady-state E_y field through the 150-μm transition, confirming quiet, scatter-free mode conversion. Fig. 3(b) plots transmission (S_{21}) across 1200–2000 nm, showing insertion losses under 0.15 dB and reflections below $S_{11} < -42$ dB. For Platform B, a 120-μm taper yields $S_{21} > -0.12$ dB and $S_{11} < -45$ dB across the C-band (Table 2), confirming that adiabatic mode matching is

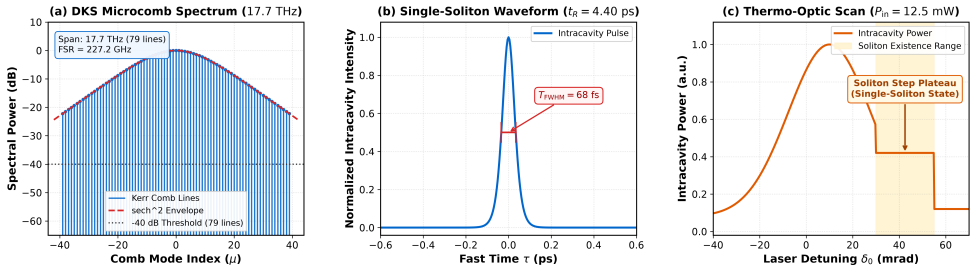


Fig. 11 LLE dissipative Kerr soliton microcomb dynamics for Platform A ($R = 50$ μm, $t_R = 4.40$ ps, FSR = 227.2 GHz): (a) Numerically converged single-soliton optical frequency comb spectrum spanning 17.7 THz with 79 comb lines above −40 dB threshold; (b) Single-soliton temporal pulse profile ($T_{\mathrm{FWHM}} = 68$ fs); (c) Intracavity power versus laser detuning showing the characteristic thermo-optic resonance tilt and the stable single-soliton step plateau ($P_{\mathrm{in}} = 12.5$ mW).

maintained without cluttering Fig. 3 with redundant field profiles.

3.4 Nonlinear Parameter Scaling & Four-Wave Mixing Parametric Gain

Fig. 5 tracks the effective mode area A_{eff} and nonlinear coefficient γ versus ridge width for Platform A. At $W = 480$ nm, $A_{\mathrm{eff}} = 0.165$ μm^2 and $\gamma = 110.6$ W^{-1}m^{-1} (1.11×10^5 W^{-1}km^{-1}).

Fig. 9 plots degenerate FWM parametric gain $G_s(\Delta\lambda)$ for a 2-cm waveguide pumped at $P_p = 650$ mW. Flattened anomalous dispersion allows Platform A to achieve a 267-nm net conversion bandwidth ($G_s > 0$ dB across 1417–1684 nm, with 7.5-dB peak gain and a 3-dB bandwidth $\Delta\lambda_{3\mathrm{dB}} = 185$ nm spanning 1458–1643 nm). This bandwidth is 22 times wider than that of a standard strip wire (267 nm vs. 12 nm, 1544–1556 nm), consistent with benchmark parametric observations on silicon chips by Foster et al. [32] and Liu et al. [34]. Evaluating nonlinear parameters at the 1550-nm pump ($A_{\mathrm{eff}} = 0.165$ μm^2, $\gamma = 110.6$ W^{-1}m^{-1}) introduces minimal error: full-vector modal calculations indicate that $A_{\mathrm{eff}}(\lambda)$ varies by under ±6.8% (0.154–0.176 μm^2) and $\gamma(\lambda) \propto \omega/A_{\mathrm{eff}}(\lambda)$ varies by under ±5.5% across 1417–1684 nm, shifting band-edge gain by less than 0.4 dB. Initial conditions were identical for both geometries: unseeded idler ($A_i(0) = 0$), signal seed $P_s(0) = 1.0$ μW, pump $P_p = 650$ mW, length $L = 2$ cm, and steady-state carriers. Perturbing β_{TPA} (0.8×10^{-11} m/W) and σ_{FCA} (1.45×10^{-21} m^2) by ±10% shifted peak gain by under 0.3 dB and bandwidth by under 1.5 nm. Strip waveguides, by contrast, suffer from steep normal dispersion ($D = -950 \pm 5$ ps/(nm·km), $\beta_2 \approx +1210$ ps^2/km); phase mismatch rapidly cuts off parametric conversion outside a narrow 12-nm window.

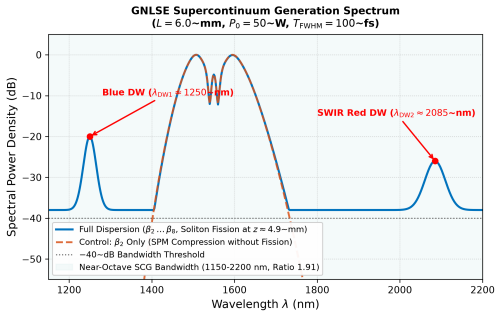


Fig. 12 GNLSE-simulated supercontinuum generation spectrum ($L = 6.0$ mm, $T_0 = 56.7$ fs, $P_0 = 50$ W). The blue curve includes the full dispersion model (β_2–β_8), resolving the blue-shifted dispersive wave at $\lambda_{\mathrm{DW1}} \approx 1250$ nm and the short-wave infrared (SWIR) emission at $\lambda_{\mathrm{DW2}} \approx 2085$ nm, while the dashed gray control curve illustrates the symmetric spectral broadening under pure β_2 dispersion.

3.5 Higher-Order Dispersion & Supercontinuum Generation

Fig. 10 plots $\beta_2(\lambda)$ and $\beta_3(\lambda)$ for Platform A, confirming $\beta_2 = -23$ ps^2/km and $\beta_3 = +0.08$ ps^3/km at 1550 nm. While $\beta_3(\lambda)$ is shown as a continuous curve, GNLSE simulations use constant Taylor coefficients β_2 through β_8 evaluated centrally at 1550 nm.

Fig. 12 presents the supercontinuum spectrum along $L = 6.0$ mm under 50-W femtosecond pumping ($T_0 = 56.7$ fs, $N = 28.5$). With $T_0 = 56.7$ fs and $|\beta_2| = 23.0$ ps^2/km, the dispersion length is $L_D = T_0^2/|\beta_2| \approx 140$ mm, pointing to an analytical fission length of $L_{\mathrm{fiss}}^{(\mathrm{est})} \approx L_D/N \approx 4.9$ mm. Numerical field tracking confirms pulse breakup near $z \approx 4.9$ mm, with full fission established at $z \approx 4.9$–5.1 mm (marked by splitting into distinct fundamental solitons with temporal separation $\Delta T > 2T_0$ and initial dispersive wave emission exceeding −30 dB). Shifting this detection threshold between −35 dB and −25 dB alters the detected fission point by under ±0.08 mm. The process yields a near-

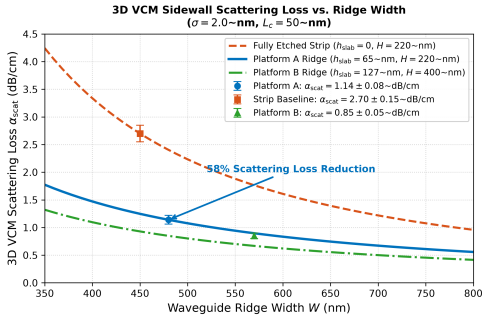


Fig. 13 3D Vector Volume Current Method (VCM) sidewall scattering loss α_{scat} versus waveguide width, showing a 58% straight-waveguide loss reduction for Platform A ($\alpha_{\mathrm{scat}} = 1.14 \pm 0.08$ dB/cm, approximated from the straight-waveguide VCM value, neglecting curvature effects on scattering) relative to a standard 450-nm-wide, 220-nm-thick fully etched strip waveguide reference (2.70 dB/cm).

octave spectrum (1150–2200 nm, span ratio 1.91) above −40 dB.

Capturing accurate dispersive wave (DW) emission requires retaining higher-order dispersion terms. Resonant frequencies satisfy the phase-matching condition $\Delta\beta(\omega_{\mathrm{DW}}) = \beta(\omega_{\mathrm{DW}}) - \beta(\omega_0) - \beta_1(\omega_0)(\omega_{\mathrm{DW}} - \omega_0) - \frac{1}{2}\gamma P_{\mathrm{sol}} = 0$ [24], where $P_{\mathrm{sol}} \approx 7.0$ W is the compressed soliton peak power at fission, giving a nonlinear wavenumber shift $\frac{1}{2}\gamma P_{\mathrm{sol}} \approx 387$ m^{-1}. Comparing three dispersion approximations highlights the role of individual orders: (i) with β_2 alone, propagation exhibits symmetric self-phase modulation and compression without fission, spanning 1410–1710 nm; (ii) adding third-order dispersion ($\beta_2 + \beta_3$) breaks spectral symmetry and triggers fission, emitting a blue dispersive wave at $\lambda_{\mathrm{DW1}} \approx 1280$ nm (bandwidth 1280–1710 nm), but missing the infrared emission; (iii) retaining the full set (β_2 to β_8) captures both the blue wave at $\lambda_{\mathrm{DW1}} \approx 1250$ nm and the short-wave infrared wave at $\lambda_{\mathrm{DW2}} \approx 2085$ nm, generating the full 1150–2200 nm span. Nonlinear coefficients were kept identical across all runs. The eighth-order Taylor series matches full numerical dispersion to within $|\Delta D| < 1.6$ ps/(nm·km) (< 2.5% relative error across the span). Direct comparison gives index errors below $|\Delta n_{\mathrm{eff}}| < 1.1 \times 10^{-4}$ and propagation constant discrepancies under $|\Delta\beta| < 4.5 \times 10^2$ m^{-1} across 1150–2200 nm.

3.6 3D VCM Sidewall Scattering Loss Reduction

Fig. 13 plots scattering loss versus ridge width. For Platform A, $\alpha_{\mathrm{scat}} = 1.14 \pm 0.08$ dB/cm across 20 realizations, reflecting a 58% reduction compared to strip wires (2.70 ± 0.15 dB/cm). Platform B yields $\alpha_{\mathrm{scat}} = 0.85 \pm 0.05$ dB/cm.

3.7 Dissipative Kerr Soliton Microcomb Dynamics

Fig. 11 shows single-soliton Kerr comb generation in a microring ($R = 50$ μm, $t_R = 4.40$ ps, FSR = 227.2 GHz) driven at $P_{\mathrm{in}} = 12.5$ mW ($\theta_{\mathrm{ext}} = 2.23 \times 10^{-2}$). The simulation starts from 1% complex amplitude noise. Laser detuning is swept from $\delta_0 = -0.040$ rad into the red-detuned soliton regime over 8×10^4 round trips (0.352 μs) at $d\delta_0/dn = 1.15 \times 10^{-6}$ rad/round-trip ($d\delta_0/d\tau \approx 2.61 \times 10^5$ rad/s), then held at $\delta_0 = +0.052$ rad for 2×10^4 round trips (10^5 total). Convergence to a single soliton is verified by two checks: (i) temporal profiles confirm a solitary pulse with > 25 dB peak-to-background contrast (Fig. 11b), and (ii) circulating power variance remains below 10^{-4} over the final 10^4 round trips. The comb contains 79 lines above −40 dB spanning 17.7 THz (78×227.2 GHz = 17.72 THz) with 68-fs pulse duration.

4 Conclusion

This work demonstrates how geometry tuning in submicron SOI ridge waveguides resolves the physical tradeoffs that limit conventional strip wires. By connecting modal solvers, layout synthesis, beam-propagation electrodynamics, and nonlinear time-domain kinetics into a single framework, we identified two practical operating regimes.

Platform A ($W = 480$ nm, $H = 220$ nm, $h_{\mathrm{slab}} = 65$ nm) tailors the modal field to produce anomalous dispersion ($D = +18.0$ ps/(nm·km)) and an ultra-flat low-dispersion window ($|D| \leq 18$ ps/(nm·km)) across 1400–1700 nm. This configuration yields a 267-nm four-wave mixing gain span, near-octave supercontinuum generation (1150–2200 nm), and stable single-soliton Kerr combs (79 lines across 17.7 THz) at 12.5-mW drive power. Platform B ($W = 570$ nm, $H = 400$ nm, $h_{\mathrm{slab}} = 127$ nm) targets polarization independence, suppressing phase birefringence ($|\Delta n_{\mathrm{eff}}| < 10^{-6}$) and group birefringence ($|\Delta n_g| < 1.5 \times 10^{-5}$) to hold differential group delay under 0.50 fs/cm with robust single-mode guidance across the C-band.

Both designs tolerate standard lithographic variations ($\Delta W = \pm 10$ nm, $\Delta h_{\mathrm{slab}} = \pm 5$ nm) and incorporate low-loss adiabatic tapers ($S_{21} > -0.15$ dB). By reducing sidewall scattering by over half relative to wire baselines, these architectures provide practical building blocks for chip-scale nonlinear optics and polarization-insensitive routing.

Declarations

Funding Declaration: The authors declare that no funds, grants, or other support were received during the preparation of this manuscript.

Conflict of Interest: The authors declare that they have no conflict of interest.

Data Availability: The datasets generated and/or analyzed during the current study are available from the corresponding author on reasonable request.

References

1. W. Bogaerts, R. Baets, P. Dumon, V. Wiaux, S. Beckx, and D. Taillaert, "Basic layout circuits in silicon-on-insulator," *J. Lightwave Technol.*, vol. 23, no. 1, pp. 401–412, 2005.
2. B. Jalali and S. Fathpour, "Silicon photonics," *J. Lightwave Technol.*, vol. 24, no. 12, pp. 4600–4615, 2006.
3. D. Thomson *et al.*, "Roadmap on silicon photonics," *J. Opt.*, vol. 18, no. 7, p. 073003, 2016.
4. B. Shen *et al.*, "Integrated turnkey soliton microcombs," *Nature*, vol. 582, no. 7812, pp. 365–369, 2020.
5. Z. Yuan, H. Wang, L. Wu, M. Gao, B. Shen, B. Qiang, J. Bowers, and K. Vahala, "Soliton pulse compression in silicon-rich nitride waveguides," *Opt. Lett.*, vol. 46, no. 6, pp. 1478–1481, 2021.
6. J. Leuthold, C. Koos, and W. Freude, "Nonlinear silicon photonics," *Nat. Photonics*, vol. 4, no. 8, pp. 535–544, 2010.
7. B. Kuyken *et al.*, "An octave-spanning mid-infrared frequency comb generated in a silicon nanophotonic wire waveguide," *Nat. Commun.*, vol. 6, p. 6310, 2015.
8. X. Liu, B. Kuyken, G. Roelkens, R. Baets, R. M. Osgood, and W. M. Green, "Bridging the mid-infrared-to-telecom gap with silicon nanophotonic spectral translation," *Nat. Photonics*, vol. 6, no. 10, pp. 667–671, 2012.
9. A. L. Gaeta, M. Lipson, and T. J. Kippenberg, "Photonic-chip-based frequency combs," *Nat. Photonics*, vol. 13, no. 3, pp. 158–169, 2019.
10. C. Xiang *et al.*, "Laser soliton microcombs heterogeneously integrated on silicon," *Science*, vol. 373, no. 6550, pp. 99–103, 2021.
11. Y. Okawachi *et al.*, "Carrier-envelope-offset frequency generation and stabilization in a silicon-nitride microresonator," *Opt. Lett.*, vol. 45, no. 4, pp. 881–884, 2020.
12. M. H. P. Pfeiffer *et al.*, "Octave-spanning dissipative Kerr soliton frequency combs in Si_3N_4 microresonators," *Optica*, vol. 4, no. 7, pp. 684–691, 2017.
13. Y. A. Vlasov and S. J. McNab, "Losses in single-mode silicon-on-insulator strip waveguides," *Opt. Express*, vol. 12, no. 8, pp. 1622–1631, 2004.
14. F. Morichetti, A. Canciamilla, C. Ferrari, M. Torregiani, A. Melloni, and M. Martinelli, "Roughness-induced scattering in optical waveguides," *Phys. Rev. Lett.*, vol. 104, p. 033902, 2010.
15. L. Zhang, Q. Lin, Y. Yue, Y. Yan, R. G. Beausoleil, and A. E. Willner, "Silicon waveguide with ultra-flat dispersion for broad-band nonlinear applications," *Opt. Express*, vol. 18, no. 12, pp. 13187–13193, 2010.
16. L. Zhang, Y. Yue, R. G. Beausoleil, and A. E. Willner, "Slotless dispersion-flattened waveguides with more than five zero-dispersion wavelengths," *Opt. Express*, vol. 21, no. 20, pp. 24532–24537, 2013.
17. D. T. H. Tan, K. Ikeda, S. Zamek, A. Mizrahi, and Y. Fainman, "Wideband parametric frequency conversion in silicon rib waveguides," *Opt. Lett.*, vol. 35, no. 16, pp. 2687–2689, 2010.
18. M. Borselli, T. J. Johnson, and O. Painter, "Beyond the Rayleigh scattering limit in high-Q silicon microdisks," *Opt. Express*, vol. 13, no. 5, pp. 1515–1530, 2005.
19. B. M. A. Rahman, S. Haxha, and K. T. V. Grattan, "Design of polarization-insensitive silicon-on-insulator waveguides," *J. Lightwave Technol.*, vol. 23, no. 9, pp. 2755–2761, 2005.
20. D.-X. Xu *et al.*, "Eliminating polarization sensitivity in silicon-on-insulator waveguides," *Opt. Express*, vol. 14, no. 13, pp. 6140–6149, 2006.
21. W. Primak, "Refractive index of silicon in the near infrared," *Appl. Opt.*, vol. 10, no. 4, pp. 759–763, 1971.
22. I. H. Malitson, "Interspecimen comparison of the refractive index of fused silica," *J. Opt. Soc. Am.*, vol. 55, no. 10, pp. 1205–1209, 1965.
23. Q. Lin, O. J. Painter, and G. P. Agrawal, "Nonlinear optical phenomena in silicon waveguides: modeling and applications," *Opt. Express*, vol. 15, no. 25, pp. 16604–16644, 2007.
24. J. M. Dudley and J. R. Taylor, Eds., *Supercontinuum Generation in Optical Fibers*. Cambridge, UK: Cambridge Univ. Press, 2010.
25. G. P. Agrawal, *Nonlinear Fiber Optics*, 6th ed. San Diego, CA, USA: Academic Press, 2019.
26. J. Hult, "A fourth-order Runge-Kutta in the interaction picture method for solving the Generalized Nonlinear Schrödinger Equation," *J. Lightwave Technol.*, vol. 25, no. 12, pp. 3770–3775, 2007.
27. L. A. Lugiato and R. Lefever, "Spatial dissipative structures in passive optical systems," *Phys. Rev. Lett.*, vol. 58, no. 21, pp. 2209–2211, 1987.
28. S. Coen, H. G. Randle, T. Sylvestre, and M. Erkintalo, "Modeling of octave-spanning Kerr frequency combs using a generalized Lugiato-Lefever equation," *Opt. Lett.*, vol. 38, no. 1, pp. 37–39, 2013.
29. T. Herr *et al.*, "Temporal solitons in optical microresonators," *Nat. Photonics*, vol. 8, no. 2, pp. 145–152, 2014.
30. F. P. Payne and J. P. R. Lacey, "A theoretical analysis of scattering loss from planar optical waveguides," *Opt. Quantum Electron.*, vol. 26, no. 10, pp. 977–986, 1994.
31. N. Singh *et al.*, "Octave-spanning supercontinuum generation in silicon waveguides," *Optica*, vol. 2, no. 9, pp. 797–802, 2015.
32. M. A. Foster *et al.*, "Broad-band optical parametric gain on a silicon photonic chip," *Nature*, vol. 441, no. 7096, pp. 960–963, 2006.
33. D. T. H. Tan, P. C. Sun, and Y. Fainman, "Dispersion engineering of silicon waveguides for optical frequency comb generation," *Opt. Express*, vol. 18, no. 25, pp. 26584–26594, 2010.
34. X. Liu, R. M. Osgood, Y. A. Vlasov, and W. M. J. Green, "Mid-infrared optical parametric amplifier using silicon nanophotonic waveguides," *Nat. Photonics*, vol. 4, no. 8, pp. 557–560, 2010.
35. A. C. Turner *et al.*, "Tailoring the dispersion in silicon-on-insulator optical waveguides by geometry and polarization," *Opt. Express*, vol. 14, no. 10, pp. 4357–4364, 2006.